HIGH-RESOLUTION SEISMIC VELOCITY AND ATTENUATION STRUCTURE OF THE SICHUAN-YUNNAN REGION, SOUTHWEST CHINA, USING SEISMIC CATALOG AND WAVEFORM DATA

Haijiang Zhang[1], Yunfeng Liu[1], Zhen Xu[2], Xiaodong Song[2], and Clifford H. Thurber[1]

[1]University of Wisconsin-Madison, [2]University of Illinois at Urbana-Champaign

Sponsored by Air Force Research Laboratory

Contract No. FA8718-05-C-0016

ABSTRACT

The Sichuan-Yunnan region in southwestern China lies in the transition zone between the uplifted Tibetan plateau to the west and the Yangtze continental platform to the east. This region has a very complicated geological structure and is one of the most active areas of continental earthquakes in the world. This two-year project is to develop high-resolution models of the velocity and attenuation structure of the Sichuan-Yunnan region (latitudes ~97–108^{o}E and longitudes ~21–35^{o}N) using seismic catalog and waveform data.

There are four main components in this project: (1) using waveform alignment methods (waveform cross-correlation and bispectrum analysis) to obtain more accurate differential arrival times, (2) using regional scale adaptive-grid double-difference tomography to obtain detailed P- and S-wave velocity models of the Sichuan-Yunnan region, (3) using the adaptive-grid "triple-difference" seismic attenuation method to determine the detailed attenuation structure for both Qp and Qs for this region, and (4) assembling a ground truth database.

Our current effort is to determine a high-resolution velocity model and a preliminary attenuation model for the Yunnan region using seismic catalog and waveform data. We collected catalog and waveform data from the China Seismological Bureau (newly named China Earthquake Administration), Sichuan, and Yunnan provincial bureaus, and the Incorporated Research Institute for Seismology (IRIS) data management center. We measured more accurate differential times using a waveform alignment algorithm BCSEIS. We developed regional scale adaptive-grid double-difference tomography based on tetrahedral diagrams that deals properly with the curvature of the Earth and has the ability to automatically adapt the inversion grid according to the data distribution. We also modified the code to include the function to invert the Q model using absolute and differential t* values. The absolute t* values are calculated from the amplitude spectrum based on an Ω-square source model with a single corner frequency. The differential t* values are calculated from spectral ratios for two event and station pairs in order to cancel source and site effects. Our next effort is to measure differential times and absolute and differential t* values for the Sichuan region and obtain detailed velocity and attenuation models. Finally we will assemble a ground truth database for the region of size approximately 1300 km × 1000 km.

OBJECTIVES

The routine practice of locating seismic events based on a one-dimensional velocity model inevitably introduces bias into locations. Using a high-resolution three-dimensional seismic velocity model significantly improves seismic event location accuracy and thus helps satisfy the goal of nuclear explosion monitoring. In addition to seismic event locations, seismic wave amplitudes are also important in discriminating between earthquakes and explosions. As seismic waves travel through an anelastic and heterogeneous medium, their amplitudes will be attenuated, and knowledge of the attenuation structure is vital to correct the distortion. Our research program aims to develop high-resolution models of the velocity and attenuation structure of the Sichuan-Yunnan region (latitudes ~97–108^{o}E and longitudes ~21–35^{o}N) that is located in southwest China using seismic catalog and waveform data. This research project falls in topic 2 (Seismic Calibration and Ground Truth Collection) in an effort to "develop models that calibrate earth velocity and attenuation structure." The Sichuan-Yunnan region lies in the transition zone between the uplifted Tibetan plateau to the west and the Yangtze continental platform to the east. This region has a very complicated geological structure and is one of the most active areas of continental earthquakes in the world.

Our research program consists of four components: (1) using waveform alignment methods (waveform cross-correlation and bispectrum analysis) to obtain more accurate differential arrival times, (2) using regional scale adaptive-grid double-difference tomography to obtain detailed P- and S-wave velocity models of the Sichuan-Yunnan region, (3) using the adaptive-grid "triple-difference" seismic attenuation method to determine the detailed attenuation structure for both Qp and Qs for this region, and (4) assembling a ground truth database. In this paper, we will focus on our accomplishments on the velocity and attenuation models for the Yunnan region.

RESEARCH ACCOMPLISHED

Background

The Sichuan-Yunnan region lies in an active transition zone between the Yangtze platform to the east and the Tibetan plateau to the west and is generally believed to have had its origin in the collision between the Indian plate and the Eurasian plate about 45 Ma ago. This continental collision led to active tectonic deformation on a larger scale and created a high level of seismicity. There are seven major active seismic zones (belts) in this region including Longmen Shan, Xianshuihe, Anninghe, Xiaojiang, Red River, Lancang-Gengma, and Tengchong-Longling (Chan et al., 2001). Most, but not all, of the earthquakes in these belts are associated with fault zones that are identified at the surface. Obtaining a high-resolution seismic velocity model for this region and precise earthquake locations will help delineate fault zones at depth more clearly and facilitate their association with surface fault traces. Several magnitude 7 earthquakes occurred in this region in the last twenty years. Recent examples are the 1995 Menglian earthquake (M=7.3) and the 1996 Lijiang earthquake (M=7.0).

There have been some local to regional seismic tomography studies in this region. Chan et al., (2001) and Wang et al., (2003) used both P and S arrival data from 4,625 local and regional earthquakes recorded at 174 stations to determine a three-dimensional (3D) model of the crust and upper mantle. The horizontal grid spacing was 0.5 degrees between latitudes 25–34^{o}N and longitudes 97–105^{o}E. Their findings showed that southwestern China is characterized by low average velocity in the crust and upper mantle, large crustal thickness variations, the existence of a high-conductivity layer in the crust and/or upper mantle, and a high heat flow value (Wang et al., 2003). Yang et al., (2004) conducted a simultaneous inversion to determine the velocity structure and event locations using Pg and Sg picks on 193 stations from 9,988 earthquakes during the period of 1992 to 1999. Their P-wave velocity model, with a horizontal grid spacing of 1°, shows strong heterogeneity (velocity contrast) across the faults. Liu et al. (2005) used a combination of 602 local and regional earthquakes and 102 teleseismic events to determine a 3D P-wave velocity model with a horizontal grid spacing of 0.5° for this region. They imaged a relatively low-velocity anomaly over a large region at depths of 20 to 50 km that may indicate a mechanically weak north-south tectonic belt between Tibet and Eastern China.

Waveform Cross-Correlation Using the Bispectrum (BS) Method, BCSEIS

Researchers using cross-correlation (CC) to align waveforms often choose those time delay estimates with CC coefficients above a specified threshold. For example, Schaff et al., (2002) only select those time delays with CC values larger than 0.70 and mean coherences above 0.70. The selection of an optimum threshold value for waveform cross-correlation is important but difficult. If it is set too high, then only a limited number of very accurate

differential time data are available for further analysis. If the threshold value is set too low, then many unreliable differential time estimates are used which will negatively affect the relocation and tomography results.

The BCSEIS algorithm that we adopted for measuring waveform CC times works in the third-order spectral domain and can suppress correlated Gaussian or low-skewness noise sources (Nikias and Raghuveer, 1987; Nikias and Pan, 1988). BCSEIS employs a third-order spectral method to calculate two additional time delay estimates with both the raw (unfiltered) and band-pass filtered waveforms, and uses them to verify (select or reject) the one computed with the CC technique using the filtered waveforms (Du et al., 2004a). Thus this BS verification process can reject unreliable CC time delay estimates and also can accept additional CC time delays even if their associated CC coefficients are smaller than a nominal threshold value if they pass the BS verification procedure (Du et al., 2004).

We have calculated differential times for 618 events recorded by 27 stations in Yunnan Province using BCSEIS (Figure 1). We found that the calculated differential times with different filtering are slightly different for some waveform pairs. To assure that the results are not affected by filtering, we tested several different filters. We found that the default Butterworth filter with 3 poles and 2 passes in BCSEIS changes the waveform shape around the first arrivals significantly. After testing different filtering, we decided to choose a Butterworth filter with 2 poles and 1 pass in our correlation computation. We also tested different window sizes to find a suitable one for our analysis. In total, at this point we have calculated 8,717 waveform delay times using the BCSEIS algorithm.

Figure 2 shows several examples of highly similar waveforms for pairs of events recorded at the station YS08 (the CC value is labeled at the bottom of the trace). Note that the manual picks align relatively well after the waveforms are aligned using measured relative times, verifying the quality of the hand picked absolute times. The time window we chose here is 30 samples before and 97 samples after the preliminary P arrival pick.

Double-Difference Tomography

The double-difference (DD) seismic tomography method makes use of both absolute and more accurate relative arrival times (Zhang and Thurber, 2003). DD tomography is a generalization of DD location (Waldhauser and Ellsworth, 2000); it simultaneously solves for the 3D velocity structure and seismic event locations. DD tomography uses an evolving weighting scheme for the absolute and differential arrival times in order to determine the velocity structure from larger scale to smaller scale. This method yields more accurate event locations and velocity structure near the source region than standard tomography, which uses only absolute arrival times. It has the unique ability to sharpen the velocity image near the source region because of the combination of the higher accuracy of the differential time data and the concentration of the corresponding model derivatives in the source region. The latter results from the cancellation of model derivative terms where the ray paths overlap away from the source region.

In the “sphere-in-a-box” version of DD tomography, the curvature of the Earth is explicitly taken into account. Following Flanagan et al., (2000), we solve this problem by parameterizing a spherical surface inside a Cartesian volume of grid nodes. Finite-difference ray tracing algorithms (Podvin and Lecomte, 1991) are used for calculating travel times and ray paths. We have successfully finished developing the adaptive-mesh “sphere-in-a-box” version of the DD tomography code. Previously the code had difficulty saving ray path information to adapt the inversion mesh due to the limitation of memory space (Zhang and Thurber, 2005). We overcame this challenge by modifying the code to save ray density information on an intermediate grid and then project it back to the adaptive inversion mesh.

We also modified the code by finding a way to apply the smoothing constraint to the inversion mesh. Previously, we set up an intermediate regular grid and then projected the smoothing weights on it to the inversion mesh (Zhang and Thurber, 2005). This could deteriorate the advantage of using an adaptive mesh to resolve the fine scale structure because the spatial scale of the structure is limited by the size of the intermediate grid. We now have found a way to efficiently search the natural neighbors for each inversion mesh node and are able to directly apply the first-order smoothing constraint.

The adaptive-mesh DD tomography code is further modified by also adding new nodes at the midpoints of tetrahedral edges when a tetrahedron is sampled by many rays, as determined by a threshold level. The previous strategy was to only add new nodes to the center of one tetrahedron. The new strategy will be helpful for more uniformly distributing the inversion mesh nodes.

Measurement of the Absolute t* Values

Under the assumption of an Ω-square source model, the amplitude spectrum for a given event at the observing station j can be related to the attenuation and source parameters as follows:

$$\ln(A_j(f)) = \ln(\Omega_{0j}) - \ln(1 + (f/f_c)^2) - \pi f t_j^*, \quad (1)$$

where A_j is spectral amplitude at frequency f for the event observed at station j, Ω_{0j} is the amplitude asymptote at zero frequency, f_c is corner frequency for the event, and t_j* is the attenuation parameter defined as

$$t_j^* = \int_{raypath} \frac{dr}{V_j(r)Q_j(r)}. \quad (2)$$

We fit spectral amplitude data to equation (1) within the range of frequencies with adequate signal-to-noise ratio to calculate t* values. We use the multitaper method of spectral analysis (Park et al., 1987) to calculate amplitude spectra from the windowed vertical waveforms around the P arrivals. We also estimate the noise spectra from the seismograms in a window right before the signal window.

In the traditional signal-taper analysis, portions of the waveforms of interest are excluded from analysis as a trade-off for reducing the spectral leakage. In the multitaper approach, a family of statistically independent spectral estimates is computed from a signal using a set of orthogonal tapers that are referred to as discrete prolate spheriodal sequences (DPSS). Averaging over this ensemble of spectra yields an estimate with much lower variance than that from single-taper methods. Stable spectral estimation is of importance for a robust measurement of t* values.

Figure 3 shows samples of seismograms recorded at two stations HQ11 and EY24 for two events with magnitude 3.3 and 4.0, respectively. The signal windows used for amplitude spectrum calculations are indicated by vertical lines in the figure. The corresponding multitaper spectra estimated from these seismograms are shown in Figure 4. In each panel of the figure, the calculated amplitude spectra are shown as solid lines, while the noise spectra are represented by dotted lines. The fits of spectral amplitude data to equation (1) are demonstrated with dashed lines. We obtain a set of Ω, f_c and t* values from the fits as shown in each panel of the figure (Figure 4).

Measurement of Differential t* Values Using Two Events and Two Stations

The above approach for measuring absolute t* values may potentially suffer limitations when there is significant site response at some stations. We have proposed to use two events and two stations to remove source signature and site response from the spectral amplitude. For a pair of nearby events i and j observed at a pair of nearby stations l and m, we form the ratio of ratios

$$\frac{A_{il}(f)/A_{im}(f)}{A_{jl}(f)/A_{jm}(f)} = C(r)\,\frac{\exp(-\pi f(t_{il}^* + t_{jm}^*))}{\exp(-\pi f(t_{im}^* + t_{jl}^*))}, \quad (3)$$

where C(r) is a ratio of ratios of the geometrical spreading terms (assumed to be independent of frequency), with the instrument responses and source spectral amplitudes canceling out (assuming that the radiated source spectra from a given event at two nearby stations are approximately equal). Taking the natural log, we arrive at

$$\ln\left(\frac{A_{il}(f)/A_{im}(f)}{A_{jl}(f)/A_{jm}(f)}\right) = \ln C(r) + f\pi\left((t_{jl}^* - t_{il}^*) - (t_{jm}^* - t_{im}^*)\right), \quad (4)$$

which is a linear function of frequency and can be fit to determine the observed t* difference term.

Figure 5 shows the calculated spectral ratios from the above two stations and two events. We fit spectral ratios to the linear equation (4) and get the differential t* value defined in the equation (4) as 0.0066. The differential t* value calculated directly from the measured absolute t* values is 0.0070. These two values are close; however, the measured differential t* values from spectral ratios are free from station effects and are not affected by the source

model assumption. These differential t* values can be used to solve for the Q model in a way similar to DD tomography. We note that the multitaper method also improves the robustness of spectral ratios significantly.

Velocity and Attenuation Tomographic Results

At present, we collected and analyzed more catalog data for ~3,800 events and 26 stations in the Yunnan region (Figure 1). Each selected event has at least 8 observations. There are 42,500 P and S times (50% each). We applied the regular-grid DD tomography code (0.5^o grid spacing in latitude and longitude and 5 km in depth) to this data set and the new velocity model (Figure 6a) shows different features due to better ray coverage and data quality from previous results that we reported in last year's proceedings paper. For example, the low-velocity anomaly around longitude 100^o from depths of 20 km to 50 km disappears in the new model. The arrival time residuals decrease from ~964 ms for the previous data set to ~357 ms for the new data set. We also included 8,717 P-wave waveform-derived CC times from 618 events and 26 stations in the inversion. Even with this limited number of CC times, the results are very promising (Figure 6b). In comparison, the resulting event locations show more linear features and the velocity model shows sharper velocity boundaries near faults (Figure 6b). We expect to improve the event locations and velocity model once we have more waveform CC measurements. We then applied the adaptive-mesh DD tomography code to the same data set. The new strategy of adding new nodes at the middle points of tetrahedral lines when a tetrahedron is sampled by many rays is helpful for more uniformly distributing the inversion mesh nodes. Compared to the model from the regional-grid inversion shown in Figure 6a, the new model (Figure 6c) shows more fine features due to fine inversion mesh nodes in places where there are more rays.

Figures 7a and b show horizontal slices of the P- and S-wave velocity models at depths of 15 and 35 km, respectively. Both horizontal slices and cross sections show strong lateral velocity heterogeneities, consistent with the nature of active fault zones in this region. Strong velocity contrasts are evident across major faults, such as the Xiaojiang Fault and Red River Fault (Figures 6 and 7). The relocated earthquakes show relatively well-defined vertical linear features, corresponding to major faults at the surface (Figure 7). There is a low-velocity zone between the Nujiang fault and Red River fault, corresponding to the Sanjiang Fold System. Figure 7c shows horizontal slices of the Qp model at a depth of 15 and 25 km, derived from 3873 absolute P-wave t* values for 425 events and 26 stations. This preliminary attenuation model also shows low Qp values corresponding to the low velocity anomaly between the Xiaojiang Fault and Red River Fault, consistent with thick sedimentary layers in the region. We are confident that with more t* measurements from local and regional earthquakes, we will be able to characterize the attenuation structure at much higher resolution.

CONCLUSIONS AND RECOMMENDATIONS

We have applied the adaptive-mesh "sphere-in-a-box" version of DD tomography code to the Yunnan region using catalog P and S picks and waveform CC times. Both P- and S-wave velocity models show strong velocity heterogeneities, consistent with the nature of active transition zone between the Yangtze platform to the east and the Tibetan plateau to the west. Strong velocity contrasts are evident across some major fault zones and the relocated earthquakes show relatively well-defined vertical linear features. The code is also modified to include absolute and differential t* values to determine the attenuation model.

We are in the process of measuring more waveform CC times and absolute and differential t* values for the Yunnan region. A better velocity model and a more complete attenuation model will be reported in the Seismic Research Review meeting in September. After the meeting, our focus will shift to the Sichuan region. Both velocity and attenuation models will be calculated for the Yunnan-Sichuan region.

ACKNOWLEDGEMENTS

We are grateful to Megan Flanagan for allowing us to use the FD code in our "sphere-in-a-box" version of the DD tomography code. We thank Youshun Sun for providing us his compiled picks for the Sichuan-Yunnan region.

REFERENCES

Chan, W. W., C. Y. Wang, and W. D. Mooney (2001). 3-D crustal structure in southwestern China, in *Proceedings of the 23rd Seismic Research Review: Worldwide Monitoring of Nuclear Explosions,* LA-UR-01-4454, Vol. 1: pp. 12–20.

Du, W. X., C. H. Thurber, and D. Eberhart-Phillips (2004). Earthquake relocation using cross-correlation time delay estimates verified with the bispectrum method, *Bull. Seismol. Soc. Am.* 94: 856–866.

Flanagan, M. P., S. C. Myers, C. A. Schultz, M. E. Pasyanos, and J. Bhattacharyya (2000). Three-dimensional a priori model constraints and uncertainties for improving seismic location, in *Proceedings of the 22nd Annual DoD/DOE Seismic Research Symposium: Planning for Verification of and Compliance with the Comprehensive Nuclear-Test-Ban Treaty (CTBT)*, Vol. 2, pp, 129–136.

Liu, Y., X. Xhang, J. He, F. Liu, and H. Sun (2005). Three-dimensional velocity images of the crust and upper mantle beneath the north-south zone in China, *Bull. Seismol. Soc. Am.* 95: 916–925.

Nikias, C. L. and R. Pan (1988). Time delay estimation in unknown Gaussian spatially correlated noise, *IEEE Trans. Acoust. Speech Signal Process* 36: 1,706–1,714.

Nikias, C. L. and M. R. Raghuveer (1987). Bispectrum estimation: A digital signal processing framework, in *Proc. IEEE*, Vol. 75, pp. 869–891.

Park, J., C. R. Lindberg, and F. L. Vernon III (1987). Multitaper spectral analysis of high-frequency seismograms, *J. Geophys. Res.* 92: 12,675–12,684.

Podvin, P. and I. Lecomte (1991). Finite difference computation of travel times in very contrasted velocity models: a massively parallel approach and its associated tools, *Geophys. J. Int.* 105: 271–284.

Schaff, D. P., G. H. R. Bokelmann, G. C. Beroza, F. Waldhauser, and W. L. Ellsworth (2002). High-resolution image of Calaveras Fault seismicity, *J. Geophys. Res.* 107: 2186, doi:10.1029/2001JB000633.

Waldhauser, F. and W. L. Ellsworth (2000). A double-difference earthquake location algorithm: Method and application to the northern Hayward fault, CA, *Bull. Seismol. Soc. Am.* 90: 1,353–1,368.

Wang, C.-Y., W. W. Chan, and W. D. Mooney (2003). Three-dimensional velocity structure of crust and upper mantle in southwestern China and its tectonic implications, *J. Geophys. Res.* 108: 2442, doi:10.1029/2002JB001973.

Yang, Z.-X., X.-W. Yu, Y.-J. Zheng, Y.-T. Chen, X.-X. Ni, and W. Chan (2004). Earthquake relocation and 3-dimensional crustal structure of P-wave velocity in central-western China, *Acta Seismologica Sinica* 17: 20–30.

Zhang, H. and C. H. Thurber (2003). Double-difference tomography: The method and its application to the Hayward fault, California, *Bull. Seismol. Soc. Am.* 93: 1,875–1,889.

Zhang, H. and C. H. Thurber (2005). Adaptive mesh seismic tomography based on tetrahedral and Voronoi diagrams: Application to Parkfield, California, *J. Geophys. Res.* 110, B04303, doi:10.1029/2004JB003186.

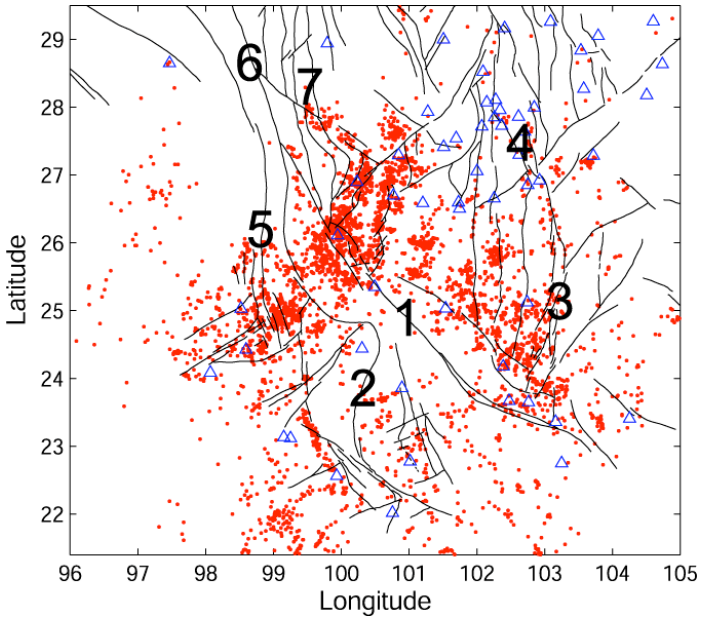

Figure 1. Location of mapped faults (black lines) in the Yunnan region. Earthquakes (red dots) are relocated using the double-difference tomography method with waveform cross-correlation differential times. Triangles indicate the local network stations.

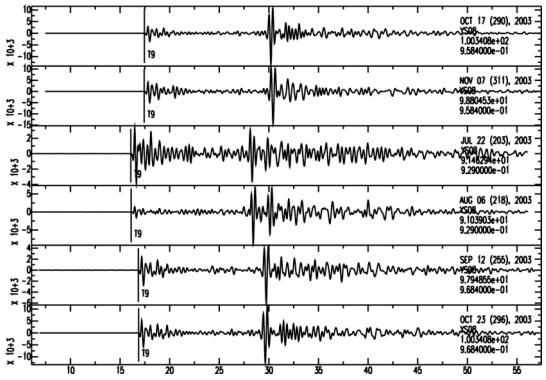

Figure 2. Similar waveforms observed on station YS08 aligned by CC times.

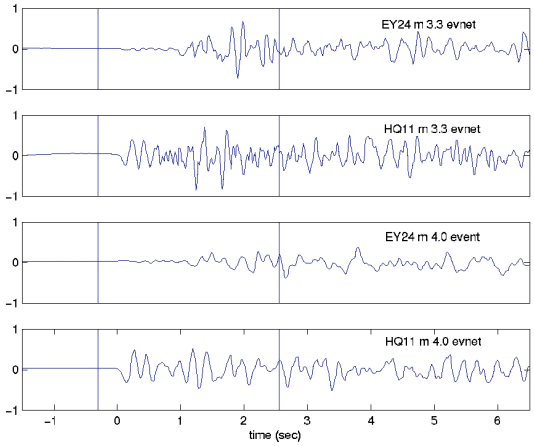

Figure 3. Waveforms at two nearby stations EY24 and HQ11 from two nearby events.

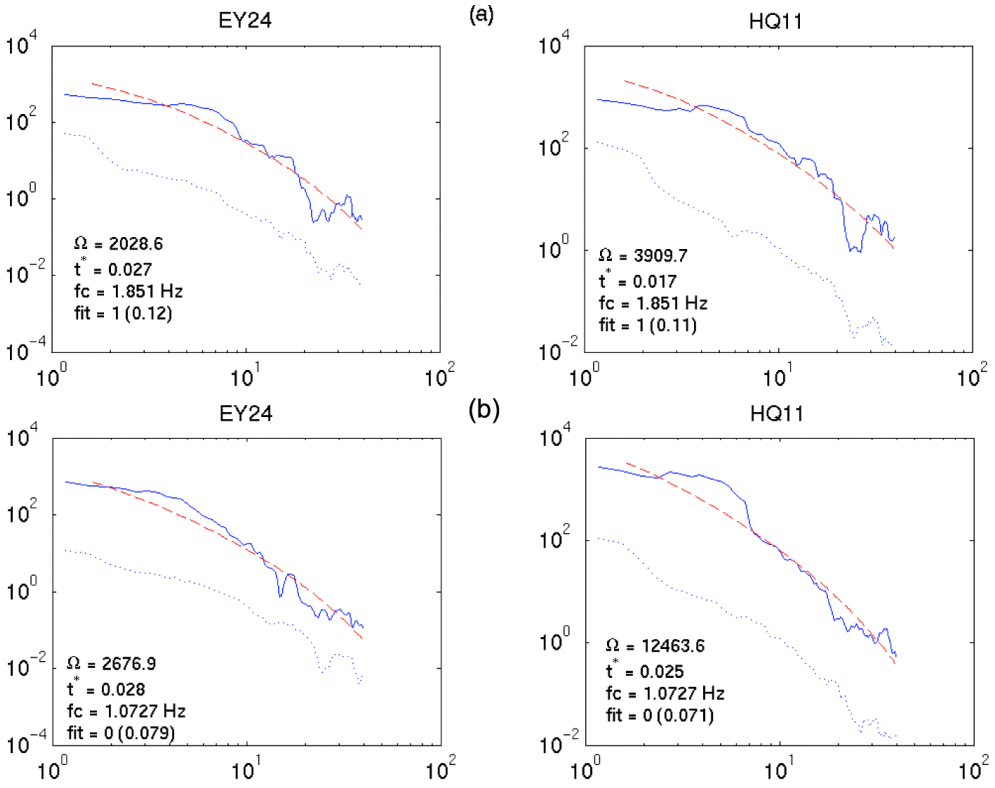

Figure 4. Spectral fitting based on Equation 1 to estimate t* values. Blue solid line: original spectra. Red dashed line: fitting spectra. Blue dots: noise spectra.

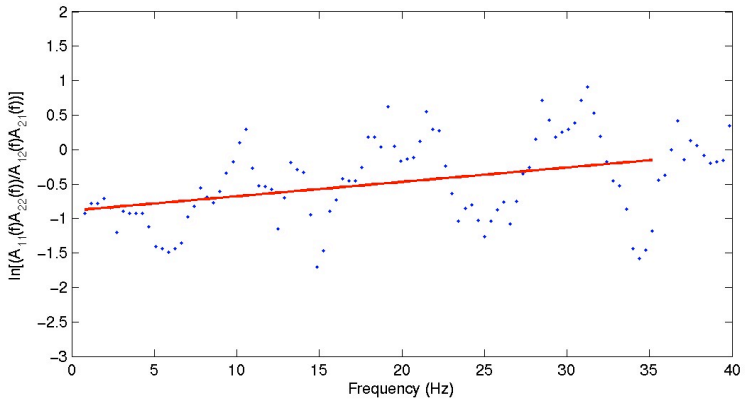

Figure 5. Differential t* measurements using spectral ratios for two events and two stations shown in Figure 4.

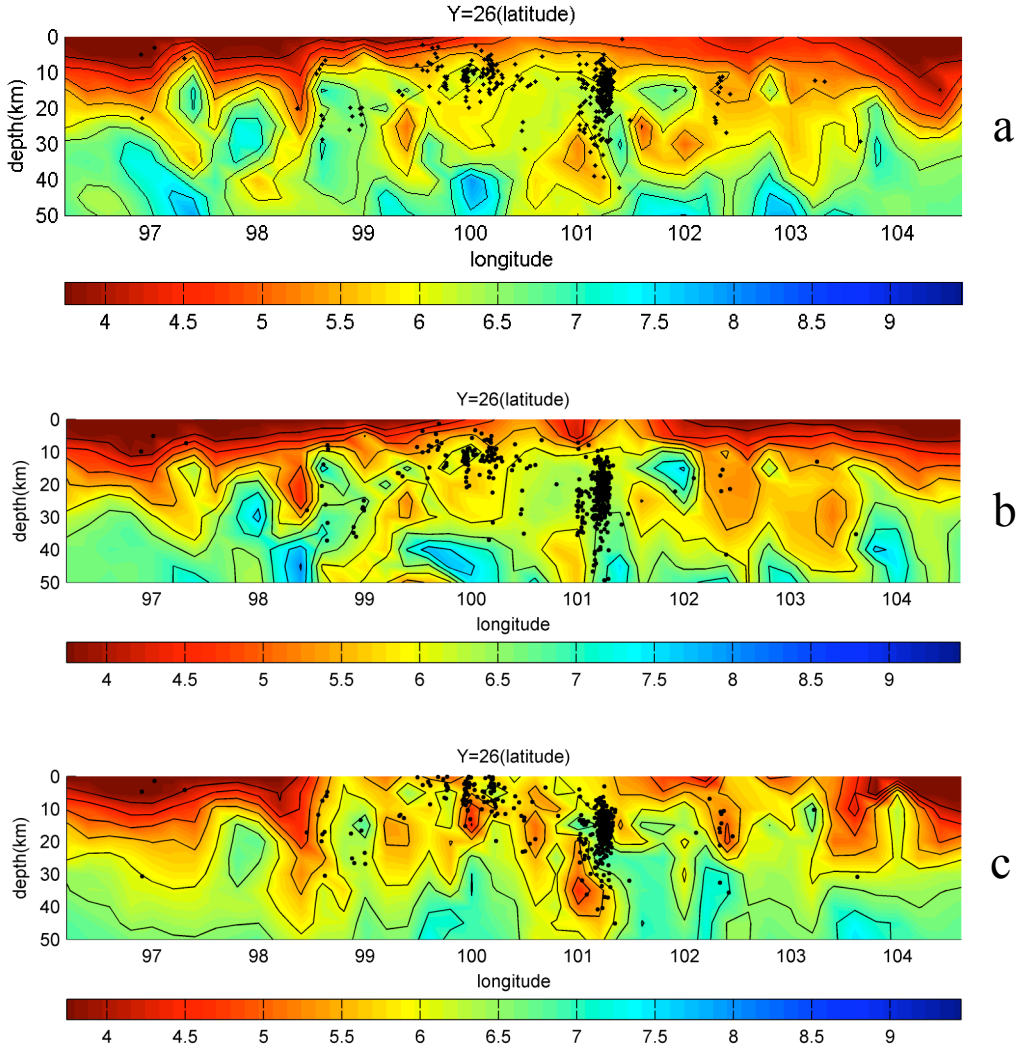

Figure 6. Cross-sections of P-wave velocity model at latitude of 26^{o} from applying the regular-grid DD tomography code to the (a) new catalog data set and (b) new catalog data set plus cross-correlation times and (c) from applying the adaptive-mesh DD tomography code to the new catalog data.

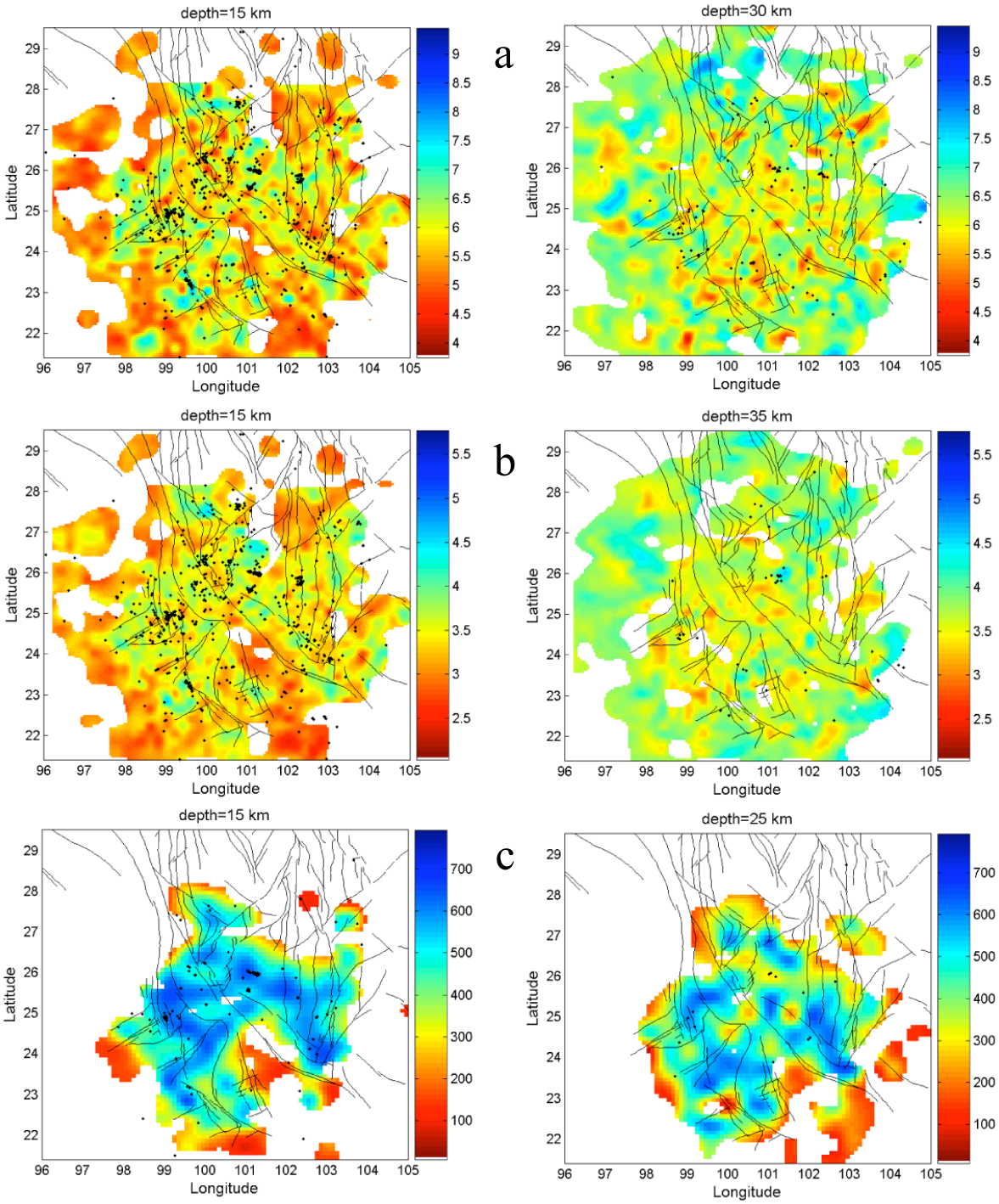

Figure 7. Map view of (a) P-wave velocity model, (b) S-wave velocity model, and (c) Q model from applying the adaptive-mesh DD tomography code to the new catalog data, at the depths indicated.